The AEPEX Mission: Imaging Energetic Particle Precipitation in the Atmosphere through its Bremsstrahlung X-ray Signatures

Robert A. Marshall[a], Wei Xu[a], Thomas Woods[b], Christopher Cully[c], Allison Jaynes[d], Cora Randall[b], Daniel Baker[b], Michael McCarthy[e], Harlan E. Spence[f], Grant Berland[a], Alexandra Wold[a], Elliott Davis[a]

[a]*Ann and H. J. Smead Department of Aerospace Engineering Sciences; University of Colorado Boulder; 3775 Discovery Drive, 429 UCB, Boulder, CO, 80303, USA*
[b]*Laboratory for Atmospheric and Space Physics; University of Colorado Boulder; 1234 Innovation Drive, Boulder, CO, 80303, USA*
[c]*Department of Physics; University of Calgary; 2500 University Drive NW, Calgary, AB, T2N 1N4, Canada*
[d]*Department of Physics & Astronomy; University of Iowa; 203 Van Allen Hall, Iowa City, Iowa, 52242, USA*
[e]*Department of Earth and Space Sciences; University of Washington; 4000 15th Avenue NE, Seattle, WA, 98195, USA*
[f]*Institute for the Study of Earth, Oceans, and Space; University of New Hampshire; 8 College Road, Durham, NH, 03824, USA*

Abstract

The Atmospheric Effects of Precipitation through Energetic X-rays (AEPEX) mission is a 6U CubeSat that will monitor energetic electron precipitation from the radiation belts into the upper atmosphere. The primary instrument will image energetic (50–300 keV) X-rays produced in the atmosphere by bremsstrahlung, providing a near-direct signature of electron precipitation. An energetic electron detector will measure the precipitating electron spectrum, while the X-ray observations will be used to determine the absolute flux. X-ray images will be produced with 10-second time resolution and 50–100 km spatial resolution. The 6U spacecraft uses flight heritage spacecraft bus subsystems, including the attitude determination and control, electrical power, and command & data handling systems. AEPEX is designed to be operated from low-Earth orbit at ∼500 km altitude with a high inclination in order to cover the outer radiation belt. AEPEX will be the first spacecraft mission to measure X-rays in the 50–300 keV energy range emitted by Earth's atmosphere in response to radiation belt precipitation, and the first to image that precipitation from above.

Keywords:
precipitation, radiation belts, bremsstrahlung, X-rays, CubeSat

1. Introduction

The Atmospheric Effects of Precipitation through Energetic X-rays (AEPEX) CubeSat mission aims to better understand the influence of the magnetosphere on the Earth's atmosphere through energetic particle precipitation (EPP). One of the key uncertainties limiting

our understanding of the impacts of EPP on the atmosphere is the lack of knowledge regarding how much energy is input to the atmosphere via EPP. To address this uncertainty, the primary objective of AEPEX is to quantify the energy deposition to the atmosphere from energetic particles that precipitate from the radiation belts.

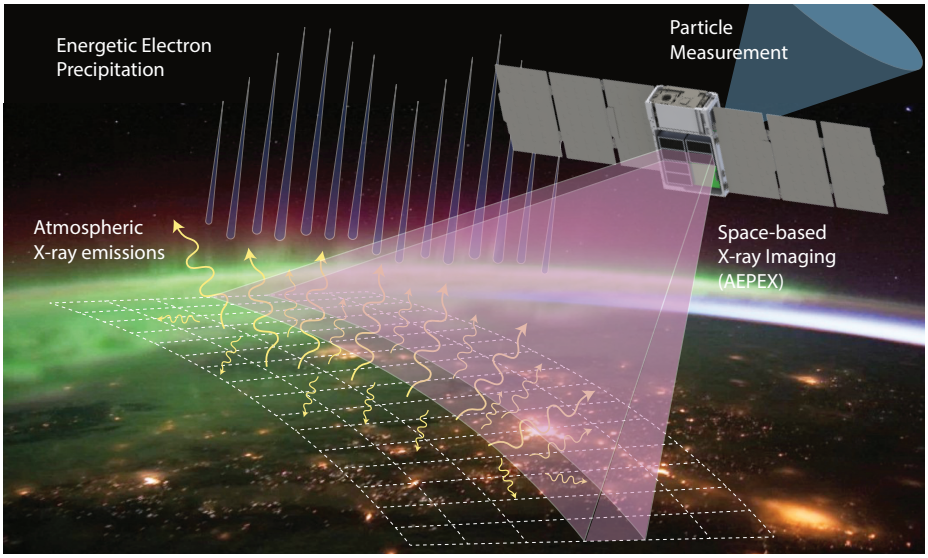

Figure 1: AEPEX will image X-rays produced by bremsstrahlung in the upper atmosphere due to energetic particle precipitation. It will thus provide measurements of the energy deposited by the precipitation and the size of precipitation regions.

The AEPEX mission will characterize the energy input into the atmosphere due to EPP during quiescent conditions as well as geomagnetic storms, substorms, and other events. It will accomplish this by a) measuring the X-ray flux emitted by the atmosphere and the precipitating electron distribution, and using these measurements to determine the precipitating flux and energy deposition; and b) imaging the X-ray emitting region to measure the spatial extent of precipitation events. Using these measurements, the AEPEX CubeSat mission will address two primary science questions. First, how much energy is deposited into the upper atmosphere through EPP, and how is it related to geomagnetic storm and substorm activity? Second, what is the spatial scale of precipitating regions during EPP events? What does this tell us about the total particle and energy flux removed from the radiation belts and deposited in the atmosphere?

AEPEX will address these questions using a novel X-ray imaging instrument, providing direct spatial measurements of energetic particle precipitation, together with a loss-cone particle detector to measure the precipitating electron spectrum. Histograms of X-ray counts will be measured with 10 second time resolution and ∼50–100 km spatial resolution, covering the high-latitude regions of the Earth's atmosphere, i.e. the radiation belts and ring current regions in LEO. These measurements will provide maps of X-ray emissions and their parent EPP fluxes on short timescales, as well as longer-term integrated emissions over the duration of substorms and geomagnetic storms, and very-long-term seasonal and MLT variations. Integrated emissions will be used to determine the total precipitating energy over the duration of these events.

1.1. Background

A comprehensive description of Sun-Earth connections requires quantifying the solar and magnetospheric energy input to the atmosphere. The energy from EPP leads initially to the production of reactive odd nitrogen ($NO_x = N + NO + NO_2$) (*Rusch et al.*, 1981) and odd hydrogen ($HO_x = H + OH + HO_2$) (*Solomon et al.*, 1981), both of which catalytically destroy ozone, a radiatively active gas. Through various dynamical and chemical processes, the absorbed energy is redistributed, and its effects amplified through such mechanisms as catalytic cycles and nonlinear wave/mean-flow interactions. Thus, EPP plays a critical role in driving the chemistry and potentially the radiative balance and circulation of the atmosphere.

1.2. Atmospheric Effects of Precipitation

In this paper, we consider "energetic" particle precipitation, EPP, those precipitating electrons and protons with energies above tens of keV. This EPP can come from the radiation belts, ring current, plasma sheet, or solar energetic particles (SEPs), as shown in Figure 2. These different sources of precipitation reach different altitudes in the atmosphere depending on their energies and incoming incident pitch angles. Of particular interest for atmospheric effects are particles that deposit their energy in the mesosphere or stratosphere; this primarily includes radiation belt and ring current electrons with energies greater than ~30 keV, and SEPs (e.g., *Thorne*, 1980; *Baker et al.*, 1987; *Sinnhuber et al.*, 2012).

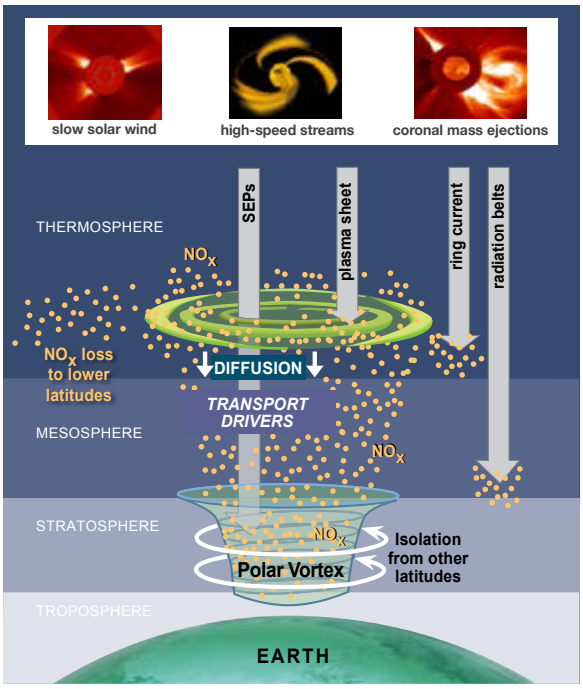

Figure 2: Energetic particle precipitation from various sources provide energy input into the upper atmosphere, producing NO_x and HO_x, which destroy ozone. The NO_x is transported to the stratosphere in polar winter, where it can have an even larger effect.

HO_x produced in the mesosphere has a short lifetime, but can cause days-long ozone depletion of up to 90% (*Andersson et al.*, 2014). NO_x produced by EPP (EPP-NO_x) directly

in the stratosphere is immediately available to participate in catalytic ozone destruction. This requires particles on the higher end of the energy spectrum and occurs only sporadically, but the effects are immediate and dramatic (e.g., *Callis et al.*, 1991; *Jackman et al.*, 2011). More commonly, EPP-NO_x is produced in the mesosphere and lower thermosphere (MLT). During the polar winter the EPP-NO_x will descend in the polar vortex into the stratosphere, where it destroys ozone (e.g., *Callis et al.*, 1998; *Randall et al.*, 2007). This mechanism for coupling the upper and lower atmosphere was first examined more than two decades ago using a 2D model (*Solomon et al.*, 1982a,b), and observational evidence for its occurrence has been prevalent (*Bailey et al.*, 2014; *Natarajan et al.*, 2004; *Randall et al.*, 1998, 2006, 2009; *Russell et al.*, 1984; *Siskind et al.*, 1997; *Siskind*, 2000).

Despite the overwhelming evidence that this is a common means by which EPP influences the atmosphere, models have been unable to simulate the effects satisfactorily. For example, in the Arctic spring of 2004, an enormous influx of EPP-NO_x was observed to descend from the MLT into the polar stratosphere (*Natarajan et al.*, 2004). NO_x mixing ratios in the upper stratosphere increased by as much as a factor of 4, causing localized catalytic reductions in ozone of more than 60% (*Randall et al.*, 2005). A number of authors have attempted to model the effects, but all underestimated the flux of EPP-NO_x into the stratosphere (see *Randall et al.*, 2015).

The model-measurement differences are striking. Figure 3 compares the observed increase in NO_x in the stratosphere and mesosphere to that simulated by the National Center for Atmospheric Research (NCAR) Whole Atmosphere Community Climate Model (WACCM), a coupled, chemistry-climate model that is widely recognized as a premier model for understanding solar and particle effects on the atmosphere (e.g., *Marsh et al.*, 2007). Note the observed enhancements in NO_x (left panel) beginning in January, which are orders-of-magnitude less significant in the WACCM results (middle panel). The discrepancy was attributed by *Randall et al.* (2015) to a combination of inaccurate specification of EPP and inadequate simulation of the vertical transport. In particular, they found that WACCM underestimated NO_x in the mesosphere between about 60 and 80 km, where electrons with energies between 50–300 keV deposit their energy (*Codrescu et al.*, 1997).

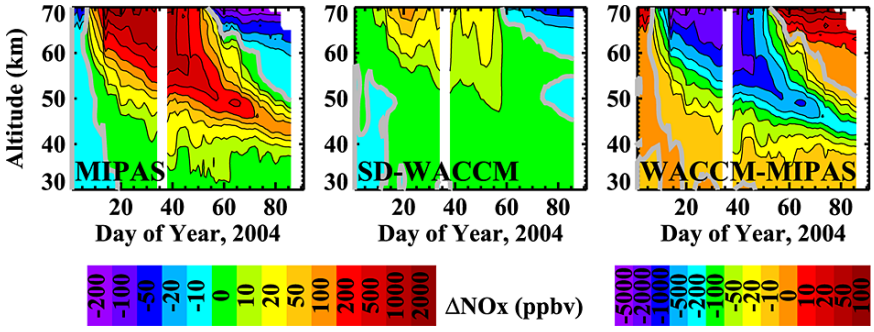

Figure 3: From *Randall et al.* (2015). (left) Differences between MIPAS NO_x measurements Jan–March 2004 and the profile measured on 1 Jan 2004. (middle) Analogous to the left plot, but for WACCM. (right) Difference between the first two panels (WACCM minus MIPAS); the thick gray contour indicates zero. Plots show 3-day running averages over the MIPAS measurement locations poleward of 70° N; white is missing data.

That WACCM would underestimate NO_x production by EPP is not surprising, since

only electrons of auroral energies were included in the model, and higher energy electrons were neglected. But the reason for this omission is that there is no satisfactory data set of higher energy electron precipitation for input to the model. The primary satellite measurements of precipitating electrons in the relevant energy range are from the NOAA POES Medium Energy Proton and Electron Detector (MEPED) (*Evans and Greer*, 2004). But these measurements suffer from proton contamination and poor spectral resolution (e.g., *Nesse Tyssøy et al.*, 2016; *Peck et al.*, 2015; *Rodger et al.*, 2010), do not adequately resolve the loss cone, and do not provide any spatial information about precipitation regions. Several authors have estimated precipitating particle flux spectra from the MEPED data, but all are accompanied by significant caveats about their validity (*Nesse Tyssøy et al.*, 2016; *Peck et al.*, 2015; *Rodger et al.*, 2010). *Smith-Johnsen et al.* (2018) showed that models are improved by adding D-region chemistry, but there are still significant model-measurement differences in simulating EEP effects. The Arctic winter of 2004, as shown in Figure 3, was remarkable with regard to the amplitude of the NO_x descent (*Randall et al.*, 2005), but such processes occur every winter at some level. AEPEX will provide an improved specification of EPP flux to use in modeling and understanding inter- and intra-seasonal variations in the atmospheric impacts of EPP.

1.3. Radiation Belt Loss and Lifetimes

EPP into the atmosphere is one of the main loss mechanisms for radiation belt electrons during the recovery phase of storms and substorms (e.g., *Li and Temerin*, 2001; *Green et al.*, 2004; *Millan and Thorne*, 2007). Understanding the lifetimes of radiation belt electrons requires an accurate specification of the losses to the atmosphere.

Most missions are unable to resolve the loss cone, and so cannot specify the complete flux that will precipitate. For example, missions in LEO such as CSSWE (*Li et al.*, 2013) measure the trapped population as well as enhancements near the loss cone edge. The POES/MEPED instruments measure only part of the loss cone; they also have limitations on energy and time resolution, as well as contamination effects (e.g., *Whittaker et al.*, 2014; *Peck et al.*, 2015). On the basis of comparisons between models and measurements for the 2003 Antarctic winter, *Pettit et al.* (2019) concluded that including energies >30 keV and the full range of pitch angles to calculate precipitating electron fluxes is necessary for improving simulations, if the simulations use in situ electron measurements as input.

On the other hand, AEPEX will measure X-rays directly produced by precipitation, and directly related to the precipitating flux. The precipitating electron spectrum will be determined by the particle detector, and will be used together with the X-ray fluxes to determine the precipitating electron flux. This will provide a much improved measurement of the loss from the radiation belts, which can then be used to inform electron loss rates and lifetimes.

1.4. Diagnostics of Energetic Precipitation

There are a number of potential methods to measure and monitor EPP in the upper atmosphere through its atmospheric signatures; a recent overview is provided by *Marshall and Cully* (2019). These signatures include i) ionization and the resulting electron density changes; ii) optical emissions, similar to auroral precipitation, but again considering higher

energy electrons; iii) direct detection of precipitating particles in-situ; iv) chemical effects, such as the production of NO_x and HO_x; or v) X-ray emissions via bremsstrahlung.

Electron density disturbances (i) can be detected by ground-based radar. Observations of EPP have been made from ground-based high-power, large aperture (HPLA) radars such as PFISR in Alaska and EISCAT in Scandinavia (*Kaeppler et al.*, 2015; *Miyoshi et al.*, 2015; *Hosokawa and Ogawa*, 2015). The advantages of HPLA detection of EPP are time resolution (1 sec) and the ability to image a single location for an extended period of time. However, radars provide only local coverage of EPP signatures, and signatures below 70 km are difficult to interpret due to the fast attachment times at these altitudes. In fact, radar observations of EPP below 70 km are rare, as free electrons attach to form cluster ions on timescales <1 ms. Nonetheless, HPLA measurements of electron density are observed below 70 km, indicating energetic precipitation. Planned conjunctions during the proposed mission will provide valuable complementary measurements to the AEPEX X-ray imaging.

Optical emissions (ii) are produced during EPP and have been predicted using Monte Carlo and transport models. Our own Monte Carlo modeling predicts that N_2^+ 1N (blue-line) signatures of ∼50 Rayleighs and O^1S (green line) signatures of ∼20 R would be expected from a precipitating flux of 10^5 electrons/cm^2/sec. However, it is likely that these optical emissions due to radiation belt precipitation would be swamped by concurrent auroral emissions.

In-situ detection of precipitating electrons (iii) provides direct observation of the energy spectrum of precipitating electrons. For EPP, measurements are best made in LEO where the loss cone is large (60° half-angle or greater); this is of course the methodology used by DEMETER, CSSWE, and other spacecraft. However, particle measurements suffer from a) inability to resolve the edge of the loss-cone, so that estimates of the precipitating flux may be inaccurate, and b) inability to measure spatial information. This latter difficulty was addressed by FIREBIRD (*Spence et al.*, 2012) and AeroCube-6 (*Turner et al.*, 2016), which can measure the spatial scale of precipitation using a pair of CubeSats. While a novel and useful technique, the spatial scales are limited by the spacecraft separation.

Many satellite instruments have detected the NO_x and HO_x chemical signatures of EPP (iv) (e.g., *Andersson et al.*, 2014; *Randall et al.*, 2005). However, none have been capable of sampling the full range of altitudes from the upper stratosphere through the MLT throughout the polar night, as would be required to infer particle input.

Baker et al. (2001) directly compared enhancements of NO_x in the lower thermosphere, observed by the Student Nitric Oxide Explorer (SNOE; *Barth et al.*, 1999), with precipitating particle fluxes (electrons with $E > 25$ keV) observed by SAMPEX (*Baker et al.*, 1993). A clear correlation is shown between enhanced particle fluxes and increases in NO_xin the altitude range between 100–160 km. The SNOE ultraviolet spectrometer was limited to a minimum altitude of 90 km, and so correlations with higher-energy electron precipitation in the mesosphere and stratosphere was not possible.

Finally, X-ray imaging of EPP (v) provides a measurement of the energy deposition and electron energy distribution, while also providing spatial information about the precipitation region. The precipitating electron distribution can be completely determined from the photon flux and energy distribution if the precipitating electron spectrum is known. Without the electron spectrum, the shape of the X-ray energy distribution can be used to constrain the EPP distribution with reasonable accuracy (see Section 2.1 below). This

method provides the best spatial coverage, and thus can be used to determine precipitating region sizes together with accurate fluxes.

1.5. Previous Measurements of Bremsstrahlung X-rays

Sample et al. (2020) provides a recent overview of measurements of radiation belt precipitation through bremsstrahlung X-rays, from orbiting platforms, high-altitude balloons, and sounding rockets. Such measurements have been carried out beginning in the 1960s and 1970s. The earliest balloon measurements were reviewed by *Parks et al.* (1993), and extend back to the first measurements of auroral X-rays by *Winckler and Peterson* (1957). The first orbital measurements of bremsstrahlung X-rays were reported by *Imhof et al.* (1974), using data from the 1972-076B satellite.

The particle environment monitor (PEM) instrument on the UARS mission (*Winningham et al.*, 1993; *Sharber et al.*, 1993; *Lummerzheim and Rees*, 1996) is the most similar to AEPEX in design. PEM included a 44 kg X-ray imaging instrument, known as AXIS, to measure X-rays from 6–150 keV emitted by the atmosphere. Other specifications for PEM/AXIS are similar to the instrument proposed here: ∼100 km spatial resolution, 16 spatial channels, and 16 energy bins. PEM/AXIS data has been used to estimate precipitating fluxes (e.g., *Chenette et al.*, 1993).

The Polar Ionospheric X-ray Imaging Experiment (PIXIE; *Imhof et al.*, 1995) flew on the POLAR spacecraft and imaged X-rays emitted by the atmosphere from 2–60 keV. PIXIE used pinhole-style cameras to detect and image X-rays and was designed to study X-ray emissions from auroral precipitation, i.e. precipitating electrons up to tens of keV. Nonetheless it did observe X-rays up to its limit of 60 keV (*Østgaard et al.*, 1999; *Petrinec et al.*, 1999).

The most recent observations of atmospheric effects of precipitation have been conducted by the BARREL balloon campaigns (*Millan et al.*, 2013; *Woodger et al.*, 2015). BARREL campaigns consist of a series of balloon launches at high latitudes to measure the X-rays produced by precipitating electrons, as well as by SEPs (*Halford et al.*, 2016). BARREL uses NaI scintillator X-ray detectors with 40 cm^2-str effective geometric factor, as balloons can carry significantly more mass and volume than a CubeSat. These detectors cover an energy range from 25 keV to 4 MeV. BARREL has an open field-of-view, which due to atmospheric absorption is effectively ∼60-degrees half-angle while looking directly at the zenith from ∼35 km altitude. Each balloon consists of a single detector, and thus do not individually provide spatial information about the precipitating region. However, multiple balloons aloft simultaneously provide spatial information related to the separation of the balloons; examples of such measurements are described in *Sample et al.* (2020).

AEPEX is a natural follow-on to these prior missions, providing the space-based measurements similar to PEM/AXIS and PIXIE, but extending the energy range up to 300 keV, including measurements of the source electron spectrum, and providing imaging of large-scale precipitation regions. The higher energy range permits a detailed study of X-rays produced by relativistic precipitation, i.e. from energetic particle populations in the radiation belt regions. These higher energies penetrate to lower altitudes, and thus have a potentially greater effect on NO_x and HO_x production.

2. Approach: Imaging Precipitation Regions

The science objectives described above will be achieved by measuring X-ray emissions from the upper atmosphere using a 6U CubeSat platform in Low-Earth Orbit (LEO). X-rays are produced in the atmosphere by bremsstrahlung when energetic electrons and protons are deflected by heavy atmospheric nuclei. These X-rays can propagate towards the ground, but are absorbed by the atmosphere above 20–30 km; a significant fraction of X-rays are scattered back towards space and can be measured from LEO. Most importantly, the energy spectrum, energy flux, spatial scales and temporal structure of X-ray emissions, measured at LEO, are directly related to the same properties of the precipitating electrons.

2.1. Inversion to Precipitating Electron Fluxes

AEPEX will measure X-rays produced by precipitating electrons; however we are primarily interested in determining the parameters of the source electrons. The AFIRE particle instrument (Section 3.2) will measure precipitating electrons in the loss cone, but because it cannot resolve the loss cone edge, there is considerable error in the true precipitating flux. AFIRE will provide a well-characterized precipitating spectrum (*Crew et al.*, 2016; *Breneman et al.*, 2017), but we must determine the precipitating flux from the X-ray observations.

The inversion from measured X-rays to precipitating electrons is an established technique dating to *Berger and Seltzer* (1972). Two methods are commonly used to conduct this inversion. The method derived by *Johns and Lin* (1992) recursively builds a matrix out of cross-section data that transforms photon spectra back into electron spectra; this matrix directly relates the observed photon spectra to incident electron spectra, and thus does not require any inversion. The second method, used by the BARREL team and described in (*Millan et al.*, 2013; *Woodger et al.*, 2015), builds a set of response functions (i.e. photon spectra) from a series of monoenergetic electron beams; the true electron spectrum is then found by determining the linear combination of monoenergetic beams that yields the best-fit photon spectrum. The method used here is most similar to this second method.

Our inversion method, shown in Figure 4, was recently published in *Xu and Marshall* (2019), and so only a brief description is provided here. A set of responses is constructed from monoenergetic electron beams; of note, the highest energy beam is chosen just above the highest energy photons observed. The observed photon spectrum — in this case, a simulated spectrum using a pre-determined electron spectrum — is then fit with a linear combination of the responses to these monoenergetic beams. Every possible combination of coefficients is tested, and the best-fit is found based on the minimization of squared residuals.

The method has been validated by comparing with the direct Monte Carlo simulation of an arbitrary precipitating electron distribution; in this case, an exponential distribution $f(E) = C_1 e^{-E/E_0}$, with $E_0 = 300$ keV. The source spectrum is shown in the middle panel of Figure 4 in black. The estimated X-ray flux and spectrum at the spacecraft are shown in the left panel (black curve). The blue curve shows the best fit to the simulated spectrum as determined from the weighted sum of X-ray responses to monoenergetic beams, and the best-fit coefficients are shown in the middle panel in red. Of importance to AEPEX, this procedure determines a best-fit using the limited photon energy range of 50–300 keV only.

An estimate of the error in the method is found through random repetition. We repeat the Monte Carlo simulation of the "observed" photon spectrum using the same electron spectrum, but selecting a different random sample from the electron distribution. The inversion process is repeated and a new set of coefficients is determined. The variation in these coefficients is illustrated in Figure 4 through the error bars on the derived electron spectrum, which denote the extreme values from 10 different simulations.

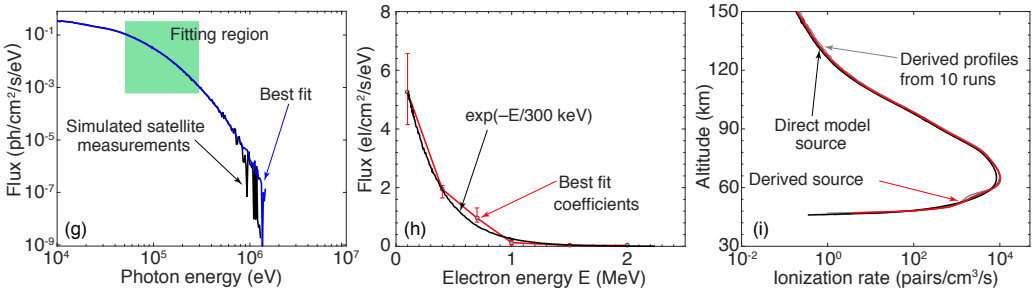

Figure 4: Inversion from X-ray measurements (left) to precipitating electron spectrum and flux (middle). The right panel shows the resulting ionization profile in the atmosphere. Adapted from (*Xu and Marshall*, 2019).

This inversion procedure has been tested on a wide range of different input distributions, including exponential, monoenergetic, uniform, and power-law distributions, each showing good inversion results. For AEPEX, we are most interested in the resulting atmospheric energy deposition. This is shown in the rightmost panel of Figure 4, for both the "true" input distribution (black), the best-fit derived distribution (red), and each of the 10 inverted distributions (grey). We observe that in every case, even at the extremes of the error bars, the atmospheric deposition profile is within 20% of the "true" profile.

Constrained Inversion. The inversion procedure shown in Figure 4 and published in *Xu and Marshall* (2019) did not use the constrained electron energy distribution; it was directly inferred from the X-ray distribution only. For AEPEX, the energy distribution will be constrained by the AFIRE instrument. To demonstrate the constrained inversion problem, we begin with a measured energy distribution with some uncertainty, as would be measured by AFIRE. Published results from *Crew et al.* (2016) and *Breneman et al.* (2017) show data from FIREBIRD that are fit to an exponential energy distribution. Simultaneous measurements from three detectors provide an uncertainty of about 10% to the e-folding factor, E_0. For example, *Crew et al.* (2016) finds $E_0 = 89$, 97, or 104 keV from three detector measurements. For this purpose, we use 97 keV as the "truth", and the other two numbers to set an uncertainty of $\sigma_{E_0} \simeq 10$ keV.

We forward-model those three exponential distributions into the atmosphere, with a flux of 10^5 electrons/cm^2/sec, producing ionization profiles and X-ray fluxes back at AEPEX altitude of 500 km. We bin the X-ray counts at AEPEX into 20% resolution bins (Figure 5a) and round each bin to an integer number of counts. We then use the X-ray flux to estimate the precipitation flux, using the method of *Xu and Marshall* (2019). For the $E_0 = 97$ keV (truth) case, we arrive at the true flux; but for the other cases ($E_0 = 89$ or 104 keV), we find an error in the estimated flux (Figure 5d) of no more than 20%.

This process is repeated for data from *Breneman et al.* (2017), and higher values of E_0 = 100, 150, 200, 250, or 300 keV, as shown in Figure 5c. In all cases the error is less than 20%, and is lower for higher E_0, thanks to a larger number of X-rays produced. We also simulated a monoenergetic precipitation with $E = 1$ MeV and 20% error in the spectral estimate (i.e, 800 keV or 1.2 MeV). In this scenario, the error in the estimated precipitation flux is 30%.

Figure 5d shows the atmospheric response in terms of ionization produced, for the 97 keV simulation. We observe that with the ∼10% error in the estimated E_0, the estimate of ionization is within 20% for all altitudes. These results demonstrate that AEPEX measurements can be used to reliably estimate the ionization production in the atmosphere.

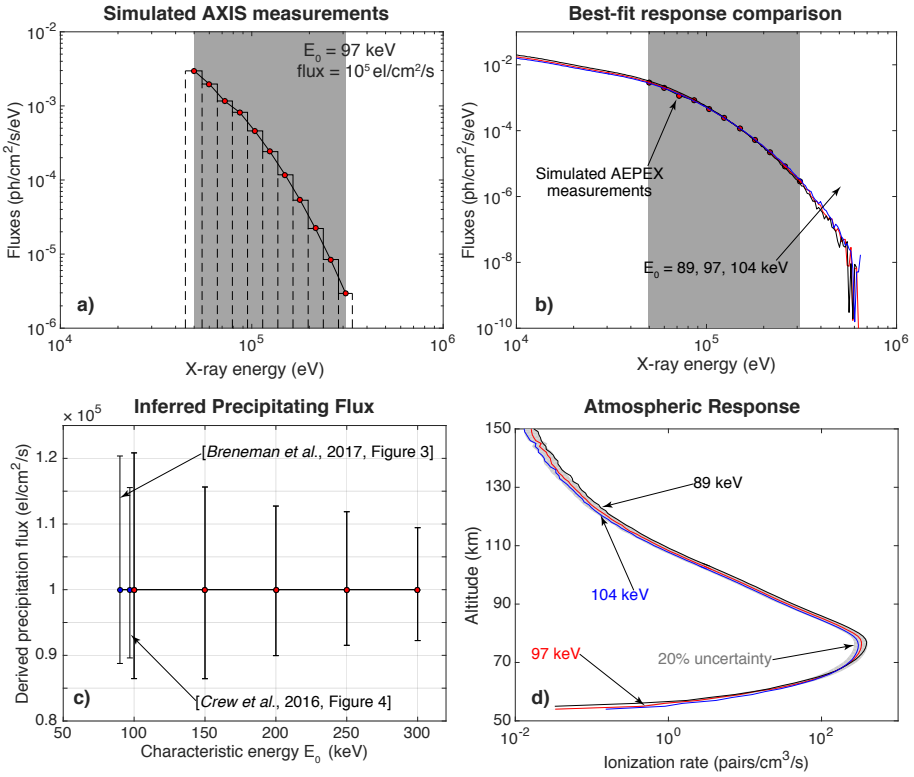

Figure 5: Inversion from electron and X-ray measurements to estimates of the flux and energy deposition.

2.2. Mission requirements

To address the science questions above, key requirements for the AEPEX mission include:

- Image X-ray emissions from the atmosphere with 200 km spatial resolution. We wish to determine the macro-scale size of precipitation regions in order to estimate the total precipitating flux during a geomagnetic event. We estimate that 200 km (about two degrees in latitude) is the minimum spatial resolution necessary to determine the precipitating region size (e.g., *Blum et al.*, 2015).

- Measure X-ray fluxes as low as 10 and as high as 10^4 photons/cm^2/str/sec. The lower limit is set by the background fluxes measured by BARREL. The upper limit is above the expected photon flux (∼6000 photons/cm^2/str/sec) from a precipitation event corresponding to the largest events observed by BARREL.
- Measure the X-ray energy distribution from 50–300 keV with 20% energy resolution. The lower limit is set to reject photons produced by auroral precipitation, typically below ∼20 keV (e.g., *Østgaard et al.*, 2001). The upper limit, determined by our inversion model described in Section 2.1, enables an accurate estimate of the precipitating electron distribution. By also directly measuring the precipitating electron spectrum, we can determine the total precipitating electron flux up to 1 MeV. The requirement of 20% energy resolution ensures a good fit to the spectrum, enabling inversion to precipitating electron flux.
- Measure the precipitating electron energy distribution from 200–1000 keV with 20% energy resolution. This is a critical range of energies for atmospheric effects of electron precipitation, and by measuring the distribution in this range we will constrain the inversion from X-rays to precipitating fluxes. The requirement of 20% energy resolution ensures a well-characterized precipitating spectrum. Electrons should be measured with a sensitivity of 10^2 electrons/cm^2/sec/str, comparable to the background levels observed in DEMETER data (e.g. *Whittaker et al.*, 2014).

These top-level requirements provide a framework from which we design the instruments, spacecraft, and mission for AEPEX.

3. Science Instruments

3.1. Atmospheric X-ray Imaging Spectrometer (AXIS)

The primary science instrument on the AEPEX CubeSat is the Atmospheric X-ray Imaging Spectrometer (AXIS). Photons are imaged onto a large detector area, providing better than 100 km spatial resolution and ∼1000 km field-of-view in both the cross-track and along-track directions.

The AXIS instrument uses an array of 12 Redlen M1770 Cadmium-Zinc-Telluride (CZT) detectors (Figure 6). Each detector has a 4 cm × 4 cm active area and a 16 × 16 array of pixels, or 256 total pixels per detector. These pixels provide more spatial resolution than necessary and more data volume than we could downlink, so data from the array will be binned onboard. Each of the 16 detectors sees the same field-of-view, and data from the detectors are combined to improve the counting statistics. Electronics boards residing behind the detectors include power regulation and instrument bias voltage power supplies, a microprocessor to collect and bin counts, and an interface to the spacecraft bus.

The Redlen M1770 CZT detector is sensitive to 50–300 keV photons. The detector has an energy resolution of 6.5% or about 3 keV at an energy of 50 keV. It can count up to 60,000 counts/sec before dead time effects become significant; with nominal 10-second exposures, and considering our geometric factor, AXIS' dynamic range is 4 $\times 10^3$. Individual photon counts are reported to the microcontroller over an SPI serial connection and include energy, pixel position, and timing information. These counts are then binned into histograms on the microcontroller with spatial and energy dimensions.

Instrument Design. The AXIS instrument design is shown in Figure 6. A single detector assembly is sufficient to provide the complete image resolution of the instrument; an array of twelve detectors are arranged to improve statistics, described below.

Each detector has an array of 16 × 16 CZT pixels, 2.2 × 2.2 mm each, with a 0.26 mm gap between each pixel. Two alternative designs were considered for the X-ray optics, each with advantages and disadvantages. The first design uses a "slit" to provide 1D imaging across the pixel array, while the other design uses a coded aperture (e.g., *Caroli et al.*, 1987). The coded aperture has the advantage of a dramatically increased aperture area, providing count rates about eight times higher than the slit design, but at the cost of increased complexity. Ultimately, the coded aperture design was selected, in order to provide higher count rates and thus a higher signal-to-noise ratio (SNR).

A 2D tungsten coded aperture is placed 20 mm above the detector array, and thin beryllium windows are placed above and below the coded aperture. The 2D aperture consists of a modified uniformly redundant array (MURA) *Fenimore and Cannon* (1978) with ∼50% effective aperture. Since this aperture provides 2D imaging, baffles are not required.

The placement of the coded aperture provides a 90 × 90 degree two-dimensional FOV, enabling true imaging of the upper atmosphere. From 500 km altitude, the spatial coverage of the atmosphere at 50 km is 930×930 km. As the spacecraft orbits at ∼7.6 km/s, successive images will overlap the previous images, and pushbroom imaging can be used to increase the SNR at the expense of time resolution. On the other hand, the same atmospheric regions will be observed continuously for about two minutes during a single pass, allowing measurements of short-scale temporal variation of EPP.

With its 90×90 degree FOV, the solid angle of the coded aperture design is 2.1 str. The coded aperture can be designed with clear aperture of 50%. A total of 1 mm of beryllium windows provide an average transmission of 97.6% for X-rays between 50–300 keV, and the detectors have a mean efficiency of 60%; thus the effective aperture is 42.8 cm^2, and the effective geometric factor of this design is 89.7 cm^2-str.

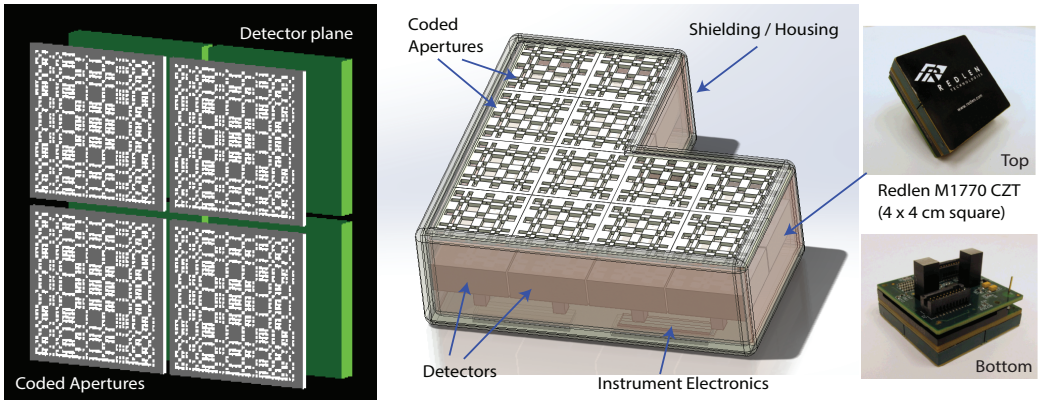

Figure 6: Left: GEANT model of a notional coded aperture (grey) above a set of four detectors (Green). Right: complete AXIS instrument with coded aperture.

Expected Photon Flux and Count Rate. To determine the expected photon flux measured by the detector array, we simulate a precipitating electron distribution, the production of photons due to bremsstrahlung in the atmosphere, the propagation of those photons to the spacecraft at 500 km altitude, and the response of the instrument to those photons.

We begin with an exponential distribution of electrons with $E_0 = 200$ keV and an integrated flux of 10^4 electrons/cm^2/sec/str above 50 keV and in the loss cone, a flux similar to the threshold that we use to count events observed by POES in Section 5.2. Electrons are propagated from an altitude of 500 km into the atmosphere using the EPMC model, which was adapted from the Monte Carlo model of *Lehtinen et al.* (1999). The model computes energy deposition, secondary ionization, and photons produced by bremsstrahlung; these photons are then propagated in the Monte Carlo code, accounting for Compton scattering and photoelectron production in the atmosphere. The atmosphere used is given by the NRLMSISE00 model (*Picone et al.*, 2002) for winter nighttime over Poker Flat, Alaska.

This simulation yields a flux of 141 photons/cm^2/sec above 50 keV and within the instrument field-of-view. Considering the average detector efficiency of 60%, the transparency of the beryllium window of 96%, the coded aperture efficiency of 50%, and the detector area of 4×4 cm, this yields a signal count rate of 657 counts/sec/detector.

Background Counts, Shielding Design, and SNR. The signal measured by the AXIS instrument will be added to background counts originating from a number of sources. First, as AEPEX flies through the radiation belts observing the X-ray signatures of precipitation, it will be heavily exposed to the precipitating electrons themselves, as well as trapped electrons mirroring between the spacecraft altitude and the atmosphere below, and backscattered electrons from the atmosphere that may be in the instrument field-of-view.

At high latitudes, AEPEX will also be exposed to Solar Energetic Protons (SEPs). However, SEPs are sporadic, occuring only during solar activity which is regularly monitored by the GOES spacecraft (e.g. *Onsager et al.*, 1996), and so the times of SEP events will be known. In addition, at all latitudes AEPEX will be exposed to Galactic Cosmic Rays (GCRs). Primary GCRs (with a flux of 10^4 cm^{-2}s^{-1}) will impact the spacecraft and produce secondaries within the spacecraft and shielding material. GCR secondaries, including X-ray photons, will be produced in the atmosphere and will enter the instrument aperture. These will form a diffuse background, but the count rate will be important in order to distinguish the signal from the background noise.

Significant shielding is required to ensure the X-ray detectors are not swamped by these background counts. The instrument housing and shielding has been designed as a graded-Z structure, with layers of polyethylene, tungsten, and tin to progressively absorb energetic electrons and photons. The polyethylene has a lower Z-number than aluminum, and is thereby designed to stop energetic electrons with minimal bremsstrahlung. The tungsten layer stops bremsstrahlung photons as much as possible, but may produce K-shell fluorescence photons at ~ 60 keV. The tin layer then absorbs those photons, and re-emits its own K-shell fluorescence at 25–30 keV. These final photons from the tin are below the energy threshold of the Redlen detectors. The specific thicknesses of the different layers will be optimized to reduce the background count rate as much as possible, while meeting mass and volume limitations for the AEPEX CubeSat.

The complete instrument structure has been simulated in GEANT4. The simula-

tion is driven with a source of electrons corresponding to the same flux and spectrum expected during a precipitation event; in particular, we use the same flux as above of 10^4 electrons/cm^2/str/sec, with an exponential energy distribution with e-folding factor $E_0 = 200$ keV. The electrons are given an sine pitch angle distribution at low-Earth orbit. The flux contributing to background counts includes electrons in the loss cone, impacting the spacecraft from above, as well as trapped electrons going downwards and upwards (i.e. electrons that mirrored below the spacecraft). Electrons backscattered from the atmosphere are included as an additional source of background counts, and the flux thereof is derived from the calculations of *Marshall and Bortnik* (2018). The simulation propagates these electrons into the instrument, and calculates secondary energetic electrons and photons produced by bremsstrahlung. Those photons are further propagated in the simulation, and can result in more energetic electrons through Compton scattering. These sources produce an average background count rate in the instrument of 77 counts/sec/detector from precipitating and trapped electrons and 24 counts/sec/detector from backscattered electrons. We observe here that the background is dominated by the GCR flux.

The background contribution of GCR proton and alpha particles are estimated using the GCR spectra from SPENVIS (*Heynderickx et al.*, 2000) at AEPEX's orbit altitude and inclination. The integral flux of protons and alphas are attenuated through the shielding, using NIST's PSTAR and ASTAR databases of material stopping power (*Berger et al.*, 1998) to determine the minimum energy particle that can penetrate the shielding. The contributions from GCR protons and alphas are found to be ~ 293 and ~ 15 counts/sec/detector, respectively. We have not included GCR secondaries produced in the spacecraft and instrument, or GCR secondaries produced by the atmosphere. These secondaries will create an additional diffuse source of background counts, which will tend to lower the SNR from the current estimate.

Adding all contributions, the total background count rate is about 408 counts/sec/detector, slightly lower than the signal count rate of 657 counts/sec/detector. A strategy has been developed to directly measure the background and increase the SNR. One of the twelve identical detectors will be used as a background detector; the coded aperture will be replaced with a tungsten plate, so that the only difference between the signal and the background detectors is the absence of the aperture. The counts and spectrum in the background detector, then, can be subtracted from the signal detectors. The signal-to-noise ratio (SNR) of the system can then be determined from

$$\mathrm{SNR} = \frac{N_{\mathrm{sig}}\Delta t}{\sqrt{(N_{\mathrm{sig}} + N_{\mathrm{bg}} + N_{\mathrm{dark}})\Delta t}} \tag{1}$$

where N_{sig} is the signal count rate, N_{bg} is the background count rate, and N_{dark} is the detector dark count rate. Laboratory testing of the Redlen detector yields an average dark count rate of $\sim$22 counts/sec over the entire detector. If we consider the numbers above on a per-detector basis, and integrate over ten seconds, we arrive at an SNR $\simeq 68$. When we combine the signals from 11 detectors, the SNR increases to $\sim$225. For imaging quality, we are also interested in the per-pixel SNR. Dividing the count rates above over 256 pixels on each detector, we find an SNR $\simeq 2.0$ on a per-pixel basis, or SNR $\simeq 6.7$ when images are averaged over the 11 detectors.

This SNR estimate will vary with the precipitating flux, the pitch angle distribution,

and due to GCR secondaries not considered. In particular, the SNR is approximately proportional to the square root of the flux, since the signal and background both increase linearly with the flux; only the GCR and dark count contribution will not change. We have simulated the SNR with different E_0, ranging from 100 to 300 keV; the SNR increases almost linearly with E_0. Future work is planned to investigate the SNR variation with different pitch angle distributions, and to estimate the SNR as a function of photon energy.

3.2. AFIRE Instrument

The AEPEX FIREBIRD Instrument for Relativistic Electrons (AFIRE) is a copy of the successful FIRE payload from the two FIREBIRD missions (*Spence et al.*, 2012; *Klumpar et al.*, 2015; *Crew et al.*, 2016). The instrument, shown in Figure 7, includes two solid-state detectors, one with a 180° FOV and one with a 45° FOV, i.e. within the loss cone. Both measure electrons from 200 keV to 1 MeV in 16 energy channels, along with an integral channel for electrons with $E > 1$ MeV (FIRE used only six energy channels in order to reduce data volume, but it is capable of 10 keV energy resolution). The two detectors have geometric factors of 9 cm^2-str (loss cone) and 23 cm^2-str (omnidirectional) and time resolution of 20 ms; these values provide sufficient sensitivity to detect and time-resolve even very weak microbursts (e.g. *Crew et al.*, 2016). This sensitivity is defined by the flux required to detect one electron in one time window; hence, using the smaller geometric factor of 9 cm^2-str and the minimum time window of 20 ms, the sensitivity is $\sim$5.5 electrons/cm^2/sec/str, easily meeting our requirement of 10^2 electrons/cm^2/sec/str.

For AEPEX, data will be binned in time to one-second histograms to reduce the data volume. The instrument uses less than 0.5U volume, weighs 252 grams, and consumes 117 mW of power during continuous operation.

Figure 7: FIRE instrument model (left) and engineering unit (right).

4. Spacecraft Design

The design of the spacecraft is driven by the size of the AXIS and AFIRE instruments. These two instruments together take up about 4U of volume, driving the need for a minimum 6U spacecraft structure. Such a spacecraft design is readily available with flight heritage; for example the TEMPEST-D mission (*Reising et al.*, 2016) flew in 2018 using a 6U spacecraft, of which 2U were taken up by the spacecraft bus components. Thus, AEPEX is designed around a 6U spacecraft design (Figure 8), with 4U allocated to the instruments.

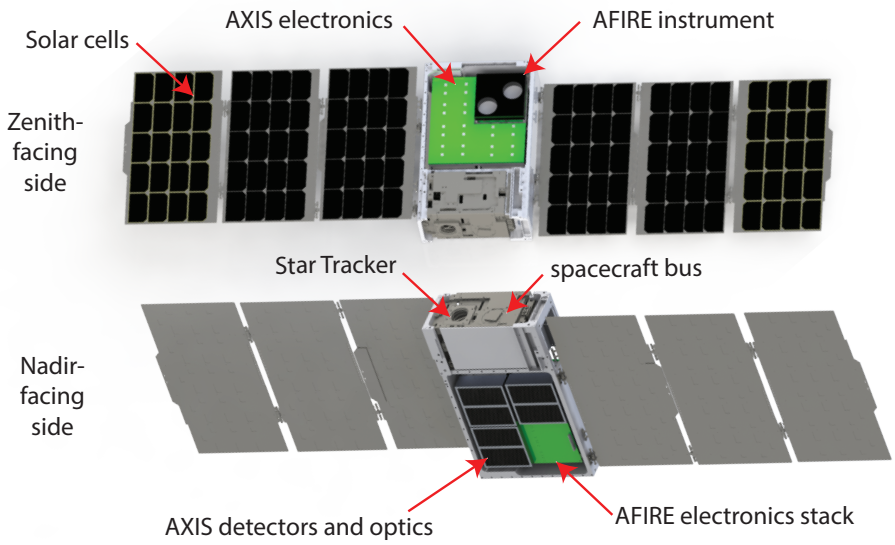

Figure 8: Nominal 6U CubeSat design, based on a 6U spacecraft structure with deployed solar panels. The AFIRE instrument will point towards the magnetic zenith while the AXIS instrument points toward magnetic nadir.

4.1. Command and Data Handling

The Command and Data Handling (CDH) subsystem controls communication between all subsystems, such as acquiring and storing instrument and subsystem telemetry data, processing and executing commands from the ground, and handling autonomous operations for spacecraft mode transitions. AEPEX CDH requirements are standard; the subsystem will collect and store data from the three AXIS detector sectors and from the AFIRE instrument. It will send this data to the S-band radio for downlink when requested. It will receive and store commands from the ground via the UHF radio.

AEPEX will use a CDH subsystem designed at built at CU Boulder with significant flight heritage. The first flight of the CU Boulder CDH was on CSSWE (*Li et al.*, 2013); versions with minor modifications have flown on MinXSS (*Mason et al.*, 2017), QB50 Challenger (*Palo et al.*, 2015), MinXSS-2, and CSIM (*Richard et al.*, 2013) CubeSats, the latter two of which were launched in late 2018.

4.2. Electrical Power System

A power budget for AEPEX has been built using best estimates of the power requirements of the instruments and spacecraft. The spacecraft bus uses an average of 10.2 W, driven primarily by the avionics, GPS receiver, and COMM system (UHF and S-band transmitters, when operating). While the AFIRE instrument uses on 130 mW on average, the AXIS instrument uses ∼15.7 W, due to the power requirements of the Redlen modules at about 1.3 W each (though they operate for only 55% of each orbit). Thus the total orbit-averaged power requirement for AEPEX is about 26 W.

To meet these power requirements, AEPEX uses deployed solar panels capable of providing a maximum of 112 W. These solar cells are connected in series to provide ∼16 V

under full illumination, which is fed to the electrical power system (EPS) electronics board. The EPS board, which has heritage from MinXSS and QB50 CubeSats, regulates the solar power to 10 V using a high-efficiency DC-DC converter; this 10 V is then used to power the other spacecraft subsystems and the instruments. A 75 Wh lithium-ion battery ensures enough power with margin for eclipse times.

The power system has been simulated in the orbit model (Section 5.1) with realistic attitudes to determine the average power generation per orbit. The spacecraft is oriented so that the solar panels are sun-pointing on the day side between latitudes of -40 and 40 degrees, i.e. around the equator where science data is not needed. The spacecraft is oriented so that the AXIS instrument is magnetic nadir-pointing (i.e. pointing downwards, along the local magnetic field line) at higher latitudes, during eclipse, and during ground station passes. This configuration provides an average power generation of 37.2 W, exceeding the average power requirement of 26 W above.

4.3. Attitude Determination and Control System

Pointing requirements for AEPEX are not stringent. We require knowledge of the spacecraft attitude to no worse than 1 degree; with the spacecraft orbiting at 500 km altitude, this maps to a location error of 8 km at 50 km altitude, where X-ray emissions originate. At $L = 6$, an error of 8 km in latitude corresponds to an error of $0.05L$, a very small error compared to typical L-shell estimatation. This requirement ensures that we are accurately locating precipitation structures in L-shell. We also require knowledge of time and location of the spacecraft to within $\sim$0.5 seconds, or half the time resolution of the AFIRE instrument, and $\sim$4 km, or half the error on the ground due to pointing error.

An existing Attitude Determination and Control System (ADCS) designed for CubeSats can provide the time, position, and pointing accuracy quite easily. AEPEX will use the XACT system from Blue Canyon Technologies (BCT). XACT has flight heritage (*Mason et al.*, 2016) and proven pointing accuracy of 0.004–0.012 degrees (3σ error) with a single star tracker (*Mason et al.*, 2017). With a built-in GPS receiver, the time and position accuracy are 100 ns and $\sim$4 m, respectively.

4.4. Communications System

Design of the communications system starts with an accurate asssessment of the data budget for the mission. We have calculated this data budget for three notional orbits: 70, 80, and 90 degree inclinations, ensuring coverage of the outer radiation belt. Both AXIS and AFIRE instruments will acquire data above latitudes of 40 degrees (south and north); in the equatorial and low-latitude regions, we do not expect to see outer radiation belt precipitation. Thus, the instruments will record for a maximum of 58% of the orbit.

With the coded aperture design, the AXIS instrument will produce 16×16-pixel images, integrated over 10 seconds, with 16 energy bins. These images will be recorded above 40 degrees latitude. Data will be averaged among the groups of four detectors, plus the single background detector. All told, the total data produced by AXIS is 149 MB/day.

AFIRE will produce spectra in 16 energy bins, from two detectors, with spectra every 1 second; again stored as 16-bit numbers, AFIRE will acquire 3.05 MB/day. Thus the total data requirement is 12.3 MB/day under the slit design, or 152 MB/day under the coded aperture design, not including housekeeping data.

AEPEX will use UHF (∼430 MHz) for uplink (commanding) and S-band (2.4 GHz) for downlink. The baseline design uses a SpaceQuest TRX-U UHF transceiver with a deployed whip antenna, a SpaceQuest TX-2400 S-band transmitter, and a Clyde Space PULSAR-SANT S-band patch antenna.

AEPEX is designed to use the UHF and S-band ground stations at LASP in Boulder, CO. The UHF ground station is capable of both uplink and downlink; it uses a Yagi antenna with 18.9 dBi gain, and operates at frequencies centered around 437 MHz. The S-band ground station is currently only capable of downlink; it uses a 4.2 m parabolic reflector at 2.4 GHz, providing 41 dBi gain.

A link budget has been developed for a 500 km altitude, with an elevation mask of 10 degrees. The UHF link budget closes with a 10 dB margin using a data rate of 9600 bps. The S-band link budget closes with 11 dB margin using a data rate of 1 Mbps. The orbit model (Section 5.1) provides an average downlink time of 25.6 minutes per day, ensuring that we can downlink up to 183 MB per day at 1 Mbps, exceeding the science data requirements for either the slit or coded aperture designs.

5. Mission Design

AEPEX is designed for a circular low-Earth orbit, with altitudes between 400 and 600 km. The lower altitude is a typical minimum, to ensure at least six months in orbit, and the upper altitude is the maximum allowable for a CubeSat to naturally de-orbit in 25 years to the atmospheric drag. The orbit altitude also drives the AXIS instrument FOV; a higher altitude creates a larger FOV, but also larger spatial resolution.

The orbit inclination requirement is driven by the need to sample regions corresponding to the outer radiation belt. Figure 9 shows a map of L-shells, covering $L = 3$ to $L = 8$. To ensure coverage down to $L = 3$ for all longitudes, we must record data at latitudes above 40 degrees. To reach $L = 8$ at all longitudes we require an orbit inclination of 85–95 degrees, since $L = 8$ reaches 85 degree latitude near -50 degrees longitude. More realistically, we can reach $L = 8$ for most longitudes with an orbit inclination of 70 or 110 degrees (red shaded region), but an inclination of 80–100 degrees is preferred (red plus green shaded regions).

The mission concept of operations has the AXIS and AFIRE instruments recording data when above 40 degree latitude, where we will cross the outer radiation belt. During science operations, the spacecraft will be oriented so that the AXIS instrument points downwards along the local magnetic field, ensuring the instrument field-of-view is centered about the magnetic field line. The AFIRE instrument, on the opposite side of the spacecraft, will point upwards along the magnetic field line. The attitude of the spacecraft will track the magnetic field as it flies through these higher latitudes. At lower latitudes on the dayside, the spacecraft will be oriented so that the solar panels face the sun. Finally, when flying over the Boulder ground station, the spacecraft attitude will track the ground station to ensure a closed link with the S-band communication system.

AEPEX will be launched as a rideshare mission, so the specific orbit is not yet known. Nonetheless, we have baselined a mission at 500 km altitude with inclinations of 70, 80, or 90 degrees for the analysis described herein.

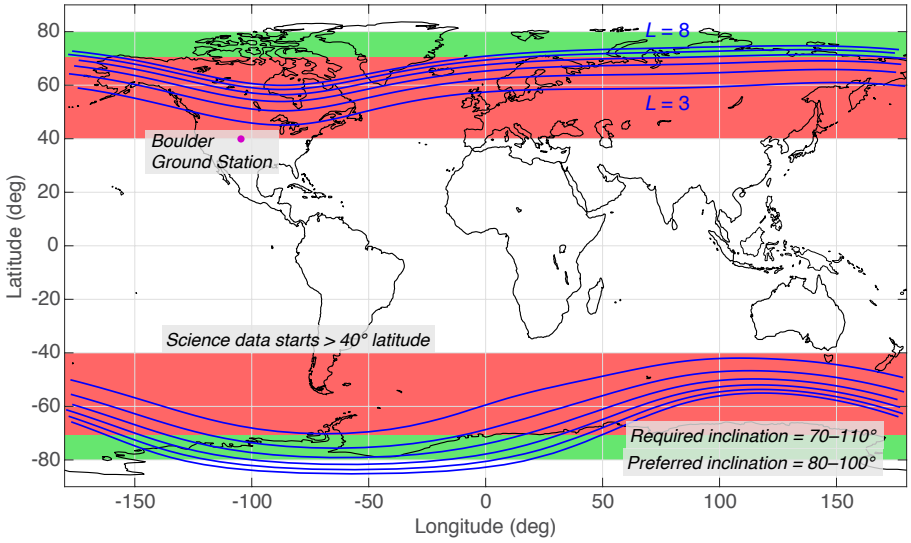

Figure 9: L-shell contours (blue) and notional latitude coverage requirements for AEPEX (red). The L-shell contours can be compared with the distribution of radiation belt observations by *Li et al.* (2013, Fig. 5).

5.1. Orbit model

An orbit model has been simulated using the Systems Took Kit (STK) software. We have simulated orbits at 500 km altitude with inclinations of 70, 80, and 90 degrees; orbits are propagated for one year to determine minima, maxima, and averages for key parameters. Figure 10 shows an example of the 90 degree (polar) orbit, simulated for one day; the orbit track is shown in blue, and the ground station coverage area (10 degree elevation mask) is shown as the yellow region around Boulder, CO.

The STK orbit models are used to estimate the orbit averaged power generation (Section 4.2), power requirements for the instruments, based on the fraction of time above 40 degrees latitude, and ground station coverage time (Section 4.4). For the three orbits simulated, these parameters do not vary significantly; nonetheless we have used the worst-case scenarios for each of these parameters in the respective discussions.

5.2. Mission Duration

The required mission duration is six months, with a possible extension to one year or longer. AEPEX aims to study precipitation during a number of geomagnetic storms and/or substorms. To estimate the expected number of these events, we analyze precipitating electron data from the POES MEPED instrument (*Peck et al.*, 2015). Figure 11 shows the fluxes of electrons $E > 50$ keV in the 0° detector of the POES MEPED instrument in 2011. Electrons in the 0° detector are definitively in the loss cone (*Nesse Tyssøy et al.*, 2016), and so these are precipitating electrons. The figure shows 38 precipitation "events" over this one-year period, which we define as sudden (< 1 day) increases in the precipitating flux above 10^3 electrons/cm^2/str/sec at $L = 5$. We estimate that during weak diffusion events, where the pitch angle distribution can be well approximated as a sine distribution, the 0° POES detector observed about 10% of the flux in the entire loss cone; hence, this 10^3 threshold for

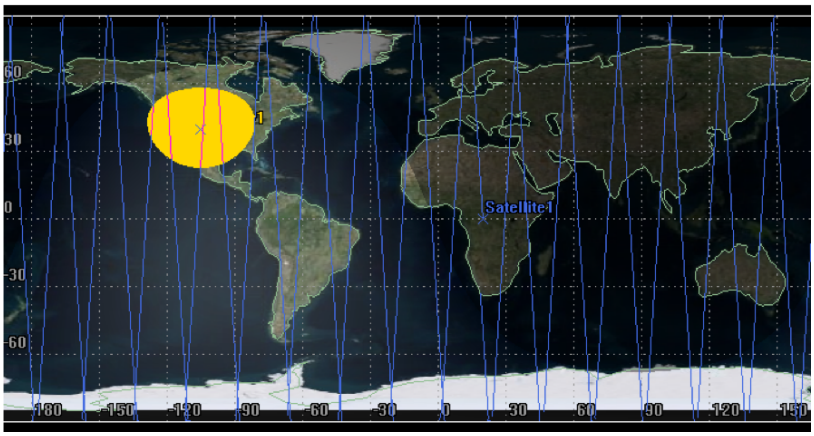

Figure 10: Notional AEPEX orbit track for one day, using a 90-degree inclination (polar) orbit. The blue line is the orbit track over ∼16 orbits; the shaded yellow region denotes the area of contact with the Boulder ground station, using a 10 degree elevation mask.

events corresponds to a loss-cone precipitating flux of 10^4 electrons/cm^2/str/sec, the value used for event modeling and SNR calculations in Section 3.1.

We have made annual plots using POES data from 1999 to 2014, covering more than one solar cycle; the results show an average of 45 events/year, and a standard deviation of 18 events/year. The minimum of 14 events occurred in 2009, at solar minimum. However, with an AEPEX launch in January 2022, solar-cycle conditions will be more similar to the 2010–2011 period (as in Figure 11), in which 28 and 38 events were observed in those two years. Thus we can reasonably expect a minimum of ∼14 events in a six-month period, with a loss-cone (precipitating) flux of at least 10^4 electrons/cm^2/str/sec.

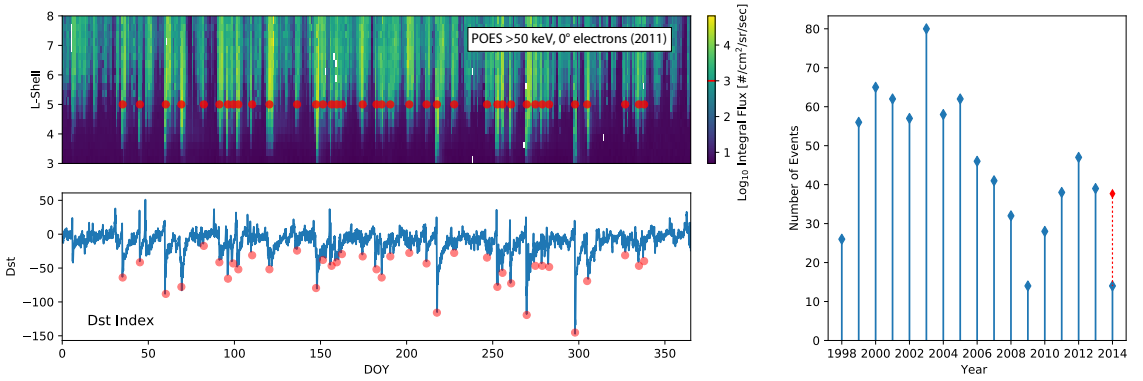

Figure 11: Top left: Fluxes of electrons $E > 100$ keV in the 0° detector of the POES MEPED instrument during 2011. "Events" are identified by red dots. Bottom left: Associated Dst index, with Dst during events highlighted with red dots. Right: events per year from 1999 to 2014; data only covers 135 days in 2014, so the red stem projects the expected number of events for the entire year.

5.3. Mission Operations Plan

There are two modes of operation for AEPEX: Safe Mode and Normal Operations (sun-pointing for battery charging is considered an aspect of normal operations). The Safe Mode is entered whenever AEPEX is activated (e.g., after launch) or as exit from Normal Operations. The instruments and ADCS are off in Safe Mode to enable the lowest possible power configuration. From MinXSS experience, the solar panels will eventually charge the battery enough through tumbling to activate the EPS regulators and thus turn on the CDH. The CDH enters Safe Mode upon startup, deploys the UHF antenna, sends out Beacon data every minute, and then autonomously exits to Normal Operations when the battery level is high enough (SOC $> 70\%$). Entry into Normal Operations turns on ADCS and deploys the solar panels after the first Sun acquisition. The instruments are typically on for Normal Operations but can be commanded off if power management is needed. The CDH will autonomously transition into Safe Mode if the battery level is low (SOC $< 50\%$).

The early orbit operations start by monitoring the Beacon data and waiting for entry into Normal Operations. This may take 1–2 days depending on battery charge level at launch. Once health and safety of the spacecraft subsystems are verified, the instruments will be activated and begin normal observations, which are expected to start about 1–2 weeks after launch. Based on MinXSS experience, there will be 2–6 contacts with the ground station per day, and most of these contacts will be automated to download the most recent housekeeping and science data.

6. Discussion and Conclusions

AEPEX represents a novel mission that will make the first measurements of hard X-rays (50–300 keV) emitted by the Earth's atmosphere. Observations will provide the first global picture of energetic electron precipitation, by observing X-rays produced during precipitation events.

We note that some tradeoffs were necessary in the mission and instrument design of AEPEX given its small size and low cost. First, the FOV of the instrument, $\sim$930 km across, limits the spatial coverage during any given pass through the radiation belts. The spatial coverage at emission altitude (50 km) results from a 90-degree FOV (full angle) and the 500 km spacecraft altitude. A higher altitude will increase this spatial coverage, at the cost of also decreasing the spatial resolution (i.e. increasing the pixel size on the atmosphere). Modification of the optical design (i.e. coded aperture spacing) can also increase the FOV, but again at the cost of spatial resolution. Furthermore, the current FOV ensures that the instrument always views inside the loss cone; a larger FOV will be exposed to trapped / mirroring radiation belt electrons, with much higher flux, increasing the noise count rate. The 1 mm-thick beryllium window in front of the baffles is designed to block incoming energetic electrons, but is not 100% effective.

Second, the slit design of the AXIS imaging system provides a small effective aperture, limiting the count rates that we expect from typical precipitation events. This optical design was chosen for its simplicity and easy of manufacturing, but requires additional detectors to increase the aperture area. The coded aperture design, commonly used in space-based X-ray imaging on much larger Astrophysics spacecraft such as INTEGRAL (*Winkler*, 1996) and Swift (e.g. *Gehrels et al.*, 2004), provides a significant increase in photon count

rates. However, a coded aperture design comes with additional complexity and difficulty in manufacturing. Furthermore, coded apertures are fundamentally a statistical imaging technique (e.g. *Caroli et al.*, 1987; *Cieślak et al.*, 2016); count rates must be reasonably high during a given exposure in order to form a useful image.

Third, the energy range of the Redlen detectors chosen for this mission is limited to just 50–300 keV; an energy range extending to 1 MeV or higher would be preferred, and would enable a better estimate of the precipitating electron spectrum. These detectors are chosen because they are available off-the-shelf, at relatively low cost, and have an integrated FPGA and ASICs which process events and determine individual photon energies with 6% energy resolution. But they were designed for laboratory X-ray imaging using the 122 keV line of Cobalt-57 as the source; they were not designed for the extended energy range that we desire. Nonetheless, we have shown in Section 2.1 that the source flux and spectrum can be inferred from this limited energy range. The compact size and off-the-shelf availability of these detectors makes them highly advantageous for the AEPEX mission.

Despite these limitations, the AEPEX CubeSat mission represents a unique opportunity to accurately measure the atmospheric effects of energetic particle precipitation, and image the precipitating regions over the globe. The mission will provide valuable measurements of EPP fluxes, and the first-ever direct observations of precipitation spatial scales. While AEPEX is focused on key science questions, a future operational spacecraft could provide continuous, global monitoring of radiation belt precipitation, providing an important measurement for operational space weather.

AEPEX was selected through the NASA H-TIDES 2018 Announcement of Opportunity. Following a Phase A Concept Study submitted in June 2019, AEPEX was selected for full implementation with a start date in December 2019. Launch is tentatively planned for Fall 2022.

7. References

Andersson, M., P. Verronen, C. Rodger, M. Clilverd, and A. Seppälä (2014), Missing driver in the Sun–Earth connection from energetic electron precipitation impacts mesospheric ozone, *Nature communications*, *5*, 5197.

Bailey, S., B. Thurairajah, C. Randall, L. Holt, D. Siskind, V. Harvey, K. Venkataramani, M. Hervig, P. Rong, and J. Russell (2014), A multi tracer analysis of thermosphere to stratosphere descent triggered by the 2013 stratospheric sudden warming, *Geophysical Research Letters*, *41*(14), 5216–5222.

Baker, D., J. Blake, D. Gorney, P. Higbie, R. Klebesadel, and J. King (1987), Highly relativistic magnetospheric electrons: A role in coupling to the middle atmosphere?, *Geophysical Research Letters*, *14*(10), 1027–1030.

Baker, D., G. M. Mason, O. Figueroa, G. Colon, J. G. Watzin, and R. M. Aleman (1993), An Overview of the Solar, Anomalous, and Magnetospheric Particle Explorer (SAMPEX) Mission, *IEEE Trans. Geosci. & Remote Sens*, *31*, 531–541.

Baker, D., C. Barth, K. Mankoff, S. Kanekal, S. Bailey, G. Mason, and J. Mazur (2001), Relationships between precipitating auroral zone electrons and lower thermospheric nitric

oxide densities: 1998–2000, *Journal of Geophysical Research: Space Physics*, *106*(A11), 24,465–24,480.

Barth, C. A., S. M. Bailey, and S. C. Solomon (1999), Solar-terrestrial coupling: Solar soft x-rays and thermospheric nitric oxide, *Geophysical research letters*, *26*(9), 1251–1254.

Berger, M. J., and S. M. Seltzer (1972), Bremsstrahlung in the atmosphere, *J. Atmos. and Terr. Phys.*, *34*(1), 85–108.

Berger, M. J., J. Coursey, M. Zucker, J. Chang, et al. (1998), *Stopping-power and range tables for electrons, protons, and helium ions*, NIST Physics Laboratory Gaithersburg, MD.

Blum, L., A. Halford, R. Millan, J. Bonnell, J. Goldstein, M. Usanova, M. Engebretson, M. Ohnsted, G. Reeves, H. Singer, et al. (2015), Observations of coincident EMIC wave activity and duskside energetic electron precipitation on 18–19 January 2013, *Geophysical Research Letters*, *42*(14), 5727–5735.

Breneman, A., A. Crew, J. Sample, D. Klumpar, A. Johnson, O. Agapitov, M. Shumko, D. Turner, O. Santolik, J. Wygant, et al. (2017), Observations directly linking relativistic electron microbursts to whistler mode chorus: Van Allen Probes and FIREBIRD II, *Geophysical Research Letters*, *44*(22), 11,265–11,272.

Callis, L. B., D. Baker, J. Blake, J. Lambeth, R. Boughner, M. Natarajan, R. Klebesadel, and D. Gorney (1991), Precipitating relativistic electrons: Their long-term effect on stratospheric odd nitrogen levels, *Journal of Geophysical Research: Atmospheres*, *96*(D2), 2939–2976.

Callis, L. B., M. Natarajan, D. S. Evans, and J. D. Lambeth (1998), Solar atmospheric coupling by electrons (SOLACE): 1. Effects of the May 12, 1997 solar event on the middle atmosphere, *Journal of Geophysical Research: Atmospheres*, *103*(D21), 28,405–28,419.

Caroli, E., J. Stephen, G. Di Cocco, L. Natalucci, and A. Spizzichino (1987), Coded aperture imaging in x-and gamma-ray astronomy, *Space Science Reviews*, *45*(3-4), 349–403.

Chenette, D., D. Datlowe, R. Robinson, T. Schumaker, R. Vondrak, and J. Winningham (1993), Atmospheric energy input and ionization by energetic electrons during the geomagnetic storm of 8–9 November 1991, *Geophysical research letters*, *20*(12), 1323–1326.

Cieślak, M. J., K. A. Gamage, and R. Glover (2016), Coded-aperture imaging systems: Past, present and future development–A review, *Radiation Measurements*, *92*, 59–71.

Codrescu, M., T. Fuller-Rowell, R. Roble, and D. Evans (1997), Medium energy particle precipitation influences on the mesosphere and lower thermosphere, *Journal of Geophysical Research: Space Physics*, *102*(A9), 19,977–19,987.

Crew, A. B., H. E. Spence, J. B. Blake, D. M. Klumpar, B. A. Larsen, T. P. O'Brien, S. Driscoll, M. Handley, J. Legere, S. Longworth, et al. (2016), First multipoint in situ observations of electron microbursts: Initial results from the NSF FIREBIRD II mission, *Journal of Geophysical Research: Space Physics*, *121*(6), 5272–5283.

Evans, D. S., and M. S. Greer (2004), Polar Orbiting Environmental Satellite Space Environment Monitor–2 Instrument Descriptions and Archive Data Documentation, *Tech. Rep. NOAA Tech. Mem. 1.4*, Space Environ. Lab., Boulder, Colorado.

Fenimore, E. E., and T. M. Cannon (1978), Coded aperture imaging with uniformly redundant arrays, *Applied optics*, *17*(3), 337–347.

Gehrels, N., G. Chincarini, P. Giommi, K. Mason, J. A. Nousek, A. Wells, N. White, S. Barthelmy, D. N. Burrows, L. Cominsky, et al. (2004), The Swift gamma-ray burst mission, *The Astrophysical Journal*, *611*(2), 1005–1020.

Green, J., T. Onsager, T. O'Brien, and D. Baker (2004), Testing loss mechanisms capable of rapidly depleting relativistic electron flux in the earth's outer radiation belt, *Journal of Geophysical Research: Space Physics*, *109*(A12211).

Halford, A., S. McGregor, M. Hudson, R. Millan, and B. Kress (2016), BARREL observations of a solar energetic electron and solar energetic proton event, *Journal of Geophysical Research: Space Physics*, *121*(5), 4205–4216.

Heynderickx, D., B. Quaghebeur, E. Speelman, and E. Daly (2000), Esa's space environment information system (spenvis)-a www interface to models of the space environment and its effects, in *38th Aerospace Sciences Meeting and Exhibit*, p. 371.

Hosokawa, K., and Y. Ogawa (2015), Ionospheric variation during pulsating aurora, *Journal of Geophysical Research: Space Physics*, *120*(7), 5943–5957.

Imhof, W., G. Nakano, R. Johnson, and J. Reagan (1974), Satellite observations of bremsstrahlung from widespread energetic electron precipitation events, *Journal of Geophysical Research*, *79*(4), 565–574.

Imhof, W., K. Spear, J. Hamilton, B. Higgins, M. Murphy, J. Pronko, R. Vondrak, D. McKenzie, C. Rice, D. Gorney, et al. (1995), The polar ionospheric X-ray imaging experiment (PIXIE), *Space Science Reviews*, *71*(1-4), 385–408.

Jackman, C., D. Marsh, F. Vitt, R. Roble, C. Randall, P. Bernath, B. Funke, M. López-Puertas, S. Versick, G. Stiller, et al. (2011), Northern hemisphere atmospheric influence of the solar proton events and ground level enhancement in january 2005, *Atmospheric Chemistry and Physics*, *11*(13), 6153–6166.

Johns, C. M., and R. Lin (1992), The derivation of parent electron spectra from bremsstrahlung hard x-ray spectra, *Solar physics*, *137*(1), 121–140.

Kaeppler, S., A. Jaynes, E. Sanchez, M. Nicolls, R. Varney, and R. Marshall (2015), Conjugate in-situ and incoherent scatter radar observations of radiation belt loss mechanisms, in *AGU Fall Meeting Abstracts*.

Klumpar, D., L. Springer, E. Mosleh, K. Mashburn, S. Berardinelli, A. Gunderson, M. Handley, N. Ryhajlo, H. Spence, S. Smith, et al. (2015), Flight system technologies enabling the twin-cubesat firebird-ii scientific mission, *Proceedings of the 29th Annual AIAA/USU Conference on Small Satellites*, (SSC15-V-6).

Lehtinen, N. G., T. F. Bell, and U. S. Inan (1999), Monte Carlo simulation of runaway MeV electron breakdown with application to red sprites and terrestrial gamma ray flashes, *J. Geophys. Res.*, *104*(A11), 24,699–24,712.

Li, X., and M. A. Temerin (2001), The electron radiation belt, *Space Science Reviews*, *95*(1-2), 569–580.

Li, X., S. Palo, R. Kohnert, L. Blum, D. Gerhardt, Q. Schiller, and S. Califf (2013), Small mission accomplished by studentsbig impact on space weather research, *Space Weather*, *11*(2), 55–56.

Lummerzheim, D., and M. Rees (1996), Validation of UARS particle environment monitor electron energy deposition, *Journal of geophysical research*, *101*(D6), 9571–9582.

Marsh, D., R. Garcia, D. Kinnison, B. Boville, F. Sassi, S. Solomon, and K. Matthes (2007), Modeling the whole atmosphere response to solar cycle changes in radiative and geomagnetic forcing, *Journal of Geophysical Research: Atmospheres*, *112*(D23306).

Marshall, R., and J. Bortnik (2018), Pitch angle dependence of energetic electron precipitation: Energy deposition, backscatter, and the bounce loss cone, *Journal of Geophysical Research: Space Physics*, *123*(3), 2412–2423.

Marshall, R. A., and C. M. Cully (2019), Atmospheric effects and signatures of high-energy electron precipitation, in *The Dynamic Loss of Earth's Radiation Belts: From Loss in the Magnetosphere to Particle Precipitation in the Atmosphere* (A. Jaynes and M. Usanova, eds.), chap. 7, pp. 199–255, Elsevier.

Mason, J. P., T. N. Woods, A. Caspi, P. C. Chamberlin, C. Moore, A. Jones, R. Kohnert, X. Li, S. Palo, and S. C. Solomon (2016), Miniature X-ray solar spectrometer: A science-oriented, university 3U CubeSat, *Journal of Spacecraft and Rockets*, *53*(2), 328–339.

Mason, J. P., M. Baumgart, B. Rogler, C. Downs, M. Williams, T. N. Woods, S. Palo, P. C. Chamberlin, S. Solomon, A. Jones, et al. (2017), MinXSS-1 CubeSat On-Orbit Pointing and Power Performance: The First Flight of the Blue Canyon Technologies XACT 3-axis Attitude Determination and Control System, *Journal of Small Satellites*, *6*, 651–662.

Millan, R., and R. Thorne (2007), Review of radiation belt relativistic electron losses, *Journal of Atmospheric and Solar-Terrestrial Physics*, *69*(3), 362–377.

Millan, R., M. McCarthy, J. Sample, D. Smith, L. Thompson, D. McGaw, L. Woodger, J. Hewitt, M. Comess, K. Yando, et al. (2013), The balloon array for RBSP relativistic electron losses (BARREL), *Space Science Reviews*, *179*(1-4), 503–530.

Miyoshi, Y., S. Oyama, S. Saito, S. Kurita, H. Fujiwara, R. Kataoka, Y. Ebihara, C. Kletzing, G. Reeves, O. Santolik, et al. (2015), Energetic electron precipitation associated with pulsating aurora: EISCAT and Van Allen Probe observations, *Journal of Geophysical Research: Space Physics*, *120*(4), 2754–2766.

Natarajan, M., E. E. Remsberg, L. E. Deaver, and J. M. Russell (2004), Anomalously high levels of NOx in the polar upper stratosphere during April, 2004: Photochemical consistency of HALOE observations, *Geophysical research letters*, *31*(L15113).

Nesse Tyssøy, H., M. Sandanger, L.-K. Ødegaard, J. Stadsnes, A. Aasnes, and A. Zawedde (2016), Energetic electron precipitation into the middle atmosphere–Constructing the loss cone fluxes from MEPED POES, *Journal of Geophysical Research: Space Physics*, *121*(6), 5693–5707.

Onsager, T., R. Grubb, J. Kunches, L. Matheson, D. Speich, R. W. Zwickl, and H. Sauer (1996), Operational uses of the goes energetic particle detectors, in *GOES-8 and Beyond*, vol. 2812, pp. 281–290, International Society for Optics and Photonics.

Østgaard, N., J. Stadsnes, J. Bjordal, R. Vondrak, S. Cummer, D. Chenette, G. Parks, M. Brittnacher, and D. McKenzie (1999), Global-scale electron precipitation features seen in UV and X rays during substorms, *Journal of Geophysical Research*, *104*(A5), 10191–10204.

Østgaard, N., J. Stadsnes, J. Bjordal, G. Germany, R. Vondrak, G. Parks, S. Cummer, D. Chenette, and J. Pronko (2001), Auroral electron distributions derived from combined UV and X-ray emissions, *J. Geophys. Res*, *106*(26), 26081–26089.

Palo, S., N. Rainville, A. Dahir, C. Rouleau, J. Stark, N. Nell, J. Fukushima, and A. Antunes de Sa (2015), One of 50: Challenger, the University of Colorado Boulder QB50 Constellation Satellite, in *AGU Fall Meeting Abstracts*.

Parks, G. K., T. J. Freeman, M. P. Mccarthy, and S. H. Werden (1993), The Discovery of Auroral XRays by Balloon-Borne Detectors and Their Contributions to Magnetospheric Research, in *Auroral Plasma Dynamics* (R.L. Lysak, ed.), *80*, 17–23.

Peck, E., C. Randall, J. Green, J. Rodriguez, and C. Rodger (2015), POES MEPED differential flux retrievals and electron channel contamination correction, *Journal of Geophysical Research: Space Physics*, *120*(6), 4596–4612.

Petrinec, S., D. Chenette, J. Mobilia, M. Rinaldi, and W. Imhof (1999), Statistical X ray auroral emissions–PIXIE observations, *Geophysical research letters*, *26*(11), 1565–1568.

Pettit, J. M., C. E. Randall, E. D. Peck, D. R. Marsh, M. van de Kamp, X. Fang, V. L. Harvey, C. J. Rodger, and B. Funke (2019), Atmospheric effects of >30 keV energetic electron precipitation in the southern hemisphere winter during 2003, *J. Geophys. Res. Space Physics*, *124*(10), 8138–8153.

Picone, J., A. Hedin, D. P. Drob, and A. Aikin (2002), NRLMSISE-00 empirical model of the atmosphere: Statistical comparisons and scientific issues, *Journal of Geophysical Research: Space Physics*, *107*(A12,1468).

Randall, C., D. Rusch, R. Bevilacqua, K. Hoppel, and J. Lumpe (1998), Polar ozone and aerosol measurement (POAM) II stratospheric NO2, 1993–1996, *Journal of Geophysical Research: Atmospheres*, *103*(D21), 28,361–28,371.

Randall, C., V. Harvey, G. Manney, Y. Orsolini, M. Codrescu, C. Sioris, S. Brohede, C. Haley, L. Gordley, J. Zawodny, et al. (2005), Stratospheric effects of energetic particle precipitation in 2003–2004, *Geophysical Research Letters*, *32*(L05802).

Randall, C., V. Harvey, C. Singleton, P. Bernath, C. Boone, and J. Kozyra (2006), Enhanced NOx in 2006 linked to strong upper stratospheric Arctic vortex, *Geophysical research letters*, *33*(L18811).

Randall, C., V. Harvey, C. Singleton, S. Bailey, P. Bernath, M. Codrescu, H. Nakajima, and J. Russell (2007), Energetic particle precipitation effects on the southern hemisphere stratosphere in 1992–2005, *Journal of Geophysical Research: Atmospheres*, *112*(D08308).

Randall, C., V. L. Harvey, D. Siskind, J. France, P. Bernath, C. Boone, and K. Walker (2009), Nox descent in the arctic middle atmosphere in early 2009, *Geophysical Research Letters*, *36*(L18811).

Randall, C. E., V. L. Harvey, L. A. Holt, D. R. Marsh, D. Kinnison, B. Funke, and P. F. Bernath (2015), Simulation of energetic particle precipitation effects during the 2003–2004 arctic winter, *J. Geophys. Res.*, *120*(6), 5035–5048.

Reising, S. C., T. C. Gaier, C. D. Kummerow, S. Padmanabhan, B. H. Lim, S. T. Brown, C. Heneghan, C. V. Chandra, J. Olson, and W. Berg (2016), Temporal experiment for storms and tropical systems technology demonstration (TEMPEST-D): Reducing risk for 6U-Class nanosatellite constellations, in *2016 IEEE International Geoscience and Remote Sensing Symposium (IGARSS)*, pp. 5559–5560, IEEE.

Richard, E., D. Harber, M. Snow, and J. Harder (2013), A compact solar spectral irradiance monitor for future small satellite and cubesat science opportunities, in *AGU Fall Meeting Abstracts*.

Rodger, C. J., M. A. Clilverd, J. C. Green, and M. M. Lam (2010), Use of POES SEM-2 observations to examine radiation belt dynamics and energetic electron precipitation into the atmosphere, *Journal of Geophysical Research: Space Physics*, *115*(A04202).

Rusch, D., J.-C. Gerard, S. Solomon, P. Crutzen, and G. Reid (1981), The effect of particle precipitation events on the neutral and ion chemistry of the middle atmospherei. odd nitrogen, *Planetary and Space Science*, *29*(7), 767–774.

Russell, J. M., S. Solomon, L. L. Gordley, E. E. Remsberg, and L. B. Callis (1984), The variability of stratospheric and mesospheric NO2 in the polar winter night observed by LIMS, *Journal of Geophysical Research: Atmospheres*, *89*(D5), 7267–7275.

Sample, J. G., R. M. Millan, and L. A. Woodger (2020), Nanosat and balloon-based studies of radiation belt loss: low-cost access to space, in *The Dynamic Loss of Earth's Radiation Belts: From Loss in the Magnetosphere to Particle Precipitation in the Atmosphere* (A. Jaynes and M. Usanova, eds.), ch. 5, pp. 121–144, Elsevier.

Sharber, J., R. Frahm, J. Winningham, J. Biard, D. Lummerzheim, M. Rees, D. Chenette, E. Gaines, R. Nightingale, and W. Imhof (1993), Observations of the UARS particle environment monitor and computation of ionization rates in the middle and upper atmosphere during a geomagnetic storm, *Geophysical research letters*, *20*(12), 1319–1322.

Sinnhuber, M., H. Nieder, and N. Wieters (2012), Energetic particle precipitation and the chemistry of the mesosphere/lower thermosphere, *Surveys in Geophysics*, *33*(6), 1281–1334.

Siskind, D. E. (2000), On the Coupling Between Middle and Upper Atmospheric Odd Nitrogen, in *Atmospheric Science Across the Stratopause* (D.E. Siskind, S.D. Eckermann and M.E. Summers, eds.), *123*, 101–116.

Siskind, D. E., J. Bacmeister, M. Summers, and J. Russell (1997), Two-dimensional model calculations of nitric oxide transport in the middle atmosphere and comparison with halogen occultation experiment data, *Journal of Geophysical Research: Atmospheres*, *102*(D3), 3527–3545.

Smith-Johnsen, C., D. R. Marsh, Y. Orsolini, H. Nesse Tyssøy, K. Hendrickx, M. I. Sandanger, L.-K. G. Ødegaard, and F. Stordal (2018), Nitric Oxide Response to the April 2010 Electron Precipitation Event: Using WACCM and WACCM-D With and Without Medium-Energy Electrons, *Journal of Geophysical Research: Space Physics*, *123*(6), 5232–5245.

Solomon, S., D. Rusch, J.-C. Gérard, G. Reid, and P. Crutzen (1981), The effect of particle precipitation events on the neutral and ion chemistry of the middle atmosphere: Ii. odd hydrogen, *Planetary and Space Science*, *29*(8), 885–893.

Solomon, S., P. J. Crutzen, and R. G. Roble (1982a), Photochemical coupling between the thermosphere and the lower atmosphere: 1. odd nitrogen from 50 to 120 km, *Journal of Geophysical Research: Oceans*, *87*(C9), 7206–7220.

Solomon, S., G. C. Reid, R. G. Roble, and P. J. Crutzen (1982b), Photochemical coupling between the thermosphere and the lower atmosphere: 2. d region ion chemistry and the winter anomaly, *Journal of Geophysical Research: Oceans*, *87*(C9), 7221–7227.

Spence, H. E., J. Blake, A. Crew, S. Driscoll, D. Klumpar, B. Larsen, J. Legere, S. Longworth, E. Mosleh, T. O'Brien, et al. (2012), Focusing on size and energy dependence of electron microbursts from the van allen radiation belts, *Space Weather*, *10*(S11004).

Thorne, R. M. (1980), The importance of energetic particle precipitation on the chemical composition of the middle atmosphere, *Pure and Applied Geophysics*, *118*(1), 128–151.

Turner, D. L., J. B. Blake, T. P. O'Brien, X. Li, and V. Angelopoulos (2016), The success of CubeSats for providing inexpensive yet high-quality observations of energetic electron precipitation from Earth's radiation belts, in *6th International HEPPA-SOLARIS Workshop Book of Abstracts*, p. 87.

Whittaker, I. C., C. J. Rodger, M. A. Clilverd, and J.-A. Sauvaud (2014), The effects and correction of the geometric factor for the POES/MEPED electron flux instrument using a multisatellite comparison, *Journal of Geophysical Research: Space Physics*, *119*(8), 6386–6404.

Winckler, J. R., and L. Peterson (1957), Large auroral effect on cosmic-ray detectors observed at 8 g/cm 2 atmospheric depth, *Physical Review*, *108*(3), 903–904.

Winkler, C. (1996), INTEGRAL. The international gamma-ray astrophysics laboratory., *Astronomy and Astrophysics Supplement Series*, *120*, 637–640.

Winningham, J., J. Sharber, R. Frahm, J. Burch, N. Eaker, R. Black, V. Blevins, J. Andrews, J. Rudzki, M. Sablik, et al. (1993), The UARS particle environment monitor, *Journal of Geophysical Research: Atmospheres*, *98*(D6), 10,649–10,666.

Woodger, L., A. Halford, R. Millan, M. McCarthy, D. Smith, G. Bowers, J. Sample, B. Anderson, and X. Liang (2015), A summary of the BARREL campaigns: Technique for studying electron precipitation, *Journal of Geophysical Research: Space Physics*, *120*(6), 4922–4935.

Xu, W., and R. A. Marshall (2019), Characteristics of energetic electron precipitation estimated from simulated bremsstrahlung x-ray distributions, *Journal of Geophysical Research: Space Physics*, *124*(4), 2831–2843.